UDC 54-31:536.413.2:537.31/32:536.758

$Nd(Ba,Sr,Ca,Mg)(Fe,Co,Cu)_2O_{6-\delta}$ LAYERED PEROVSKITES: EFFECT OF THE CONFIGURATIONAL ENTROPY ON THE STRUCTURE AND PROPERTIES

Ya.Yu. Zhuravleva[1,2], E.A. Chizhova[2*], A.S. Hlinski[3, 4], A.I. Klyndyuk[2, 5]

[1]*Department of Engineering Drawing, Belarusian State Technological University*
[2]*Department of Physical, Colloid and Analytical Chemistry, Belarusian State Technological University*
[3]*Department of Glass, Ceramic and Binding Materials Technology, Belarusian State Technological University*
[4]*Peleng JSC, Design and Production Directorate "Optical System"*
[5]*Department of Physical Chemistry and Electrochemistry, Belarusian State University*

*chizhova@belstu.by

Received 07.07.2026
Reviewed 08.07.2026
Accepted 01.09.2026

Using nitrate-citrate method the derivatives of layered neodymium–barium cobaltite with entropy stabilized barium and cobalt sublattices were synthesized, their crystal structure, oxygen nonstoichiometry, microstructure, thermal, mechanical and electrotransport properties were investigated. It was found, that increasing of configurational entropy (CE) of barium sublattice (BS) results in shrinkage of perovskite unit cell, lowering oxygen deficiency, porosity, linear thermal expansion coefficient (LTEC, α_T) and Seebeck coefficient of the samples, and increasing of their microhardness, thermal stability and electrical conductivity, which is mostly pronounced at transition from low-entropy (LE) BS to the middle-entropy (ME) one. The highest electrical conductivity and lowest LTEC value demonstrates $NdBa_{1/4}Sr_{1/4}Ca_{1/4}Mg_{1/4}Fe_{2/3}Co_{2/3}Cu_{2/3}O_{6-\delta}$ compound possessing the highest CE – ≈ 200 $S \cdot cm^{-1}$ at 1015 K and $16.2 \cdot 10^{-6}$ K^{-1} within temperature range of 350–1070 K, which is almost 10 times larger and 13 % less respectively than for $NdBaFe_{2/3}Co_{2/3}Cu_{2/3}O_{6-\delta}$ layered perovskite.

Keywords: *Layered perovskites, Configurational entropy, Oxygen nonstoichiometry, Thermal expansion, Electrical conductivity, Seebeck coefficient*

https://doi.org/10.59849/0005-2531.2026.4.77

Introduction

Complex oxides with perovskite or perovskite-like structure ($ABO_{3-\delta}$, $A_2B_2O_{6-\delta}$, $A_{n+1}B_nO_{3n+1}$, $M^IA_{n-1}B_nO_{3n+1}$ etc.) are of significant interest for researchers from different fields of science and technology as these compounds possess a number of unique magnetic, electrical, mechanical and other properties [1–5] and find application in a wide quantity of devices, including solid oxide fuel cells (SOFCs), metal-ion batteries (MIBs), thermoelectrogenerators (TEGs), gas sensors, solar cells etc. [1,3,6–7]. Among these materials, layered $REEBaCo_2O_{6-\delta}$ perovskites, where REE is rare-earth element, such as La, Pr, Nd etc., are considered as very promising cathode materials of intermediate-temperature (IT) SOFCs (IT-SOFCs) [8–10] as they exhibit high electrical conductivity and excellent

catalytic activity in oxygen reduction reaction (ORR) occurring in SOFCs [11–12]. The main disadvantage of these materials is their high LTEC values ranging from $18 \cdot 10^{-6}$ to $25 \cdot 10^{-6}$ K^{-1} [13] which is more than that of typical solid electrolytes (SEs) (10–13) 10^{-6} K^{-1} [14] and hinders the practical application of layered cobaltites. High LTEC values of $REEBaCo_2O_{6-\delta}$ phases are caused by change of spin-state of cobalt ions upon heating (from a low-spin state (Co^{III}, $t^6_{2g}e^0_g$, $S = 0$) to an intermediate- (Co^{III}, $t^5_{2g}e^1_g$, $S = 1$) and high-spin state (Co^{III}, $t^4_{2g}e^2_g$, $S = 2$) [15]. Partial substitution of cobalt by other 3*d*-metals, such as Mn, Fe, Ni etc. allows to reduce LTEC of layered cobaltites [15–18] and also, in the such cases, to improve their functional characteristics, namely, decrease the polarization resistance at the electrode/SE interface and increase the power density of the fuel cell [15,18]. The similar effect causes the partial isovalent substitution of barium by other alkaline-earth elements (AEEs) or magnesium [18–19], or of one REE by another [20–21].

Recently, new approach is being to often used based on the entropy stabilization of layered perovskites (cobaltites) through increasing of confugurational entropy (CE, ΔS_{conf}) [22–26]. The high CE values stabilize the crystal structure of complex oxides, enhance their thermal stability and improve different functional characteristics [27], resulting, for example, in decreasing of LTEC values [22] and improving electrochemical performance [24–25]. The CE values of complex oxides can be calculated using following equation:

$$\Delta S_{conf} = -R\sum_j m_j \sum_i x_{ij} \ln x_{ij}$$

where R is the gas constant, m_j is the number of atoms (ions) per formula unit in the j^{th} crystallographic site, x_{ij} is the molar fraction of i^{th} atoms (ions) in the j^{th} crystallographic site [27].

According to CE values, complex oxides can be divided into low- (LEO, $\Delta S_{conf} < 1.0R$), medium- (MEO, $1.0R < \Delta S_{conf} < 1.5R$) and high-entropy oxides (HEO, $1.5R < \Delta S_{conf}$) [27].

Earlier we had studied the efficiency of partial substitution in layered neodymium–barium ferrocuprocobaltite of barium by other AEEs or magnesium separately [28–30]. In this work the effect of CE on the structure and properties of derivatives of layered neodymium–barium cobaltite with entropy stabilized barium and cobalt sublattices was investigated.

Materials and methods

Synthesis

Samples with the composition of $NdBaFe_{2/3}Co_{2/3}Cu_{2/3}O_{5+\delta}$ (NB), $NdBa_{1/2}Sr_{1/2}Fe_{2/3}Co_{2/3}Cu_{2/3}O_{5+\delta}$ (NBS), $NdBa_{1/3}Sr_{1/3}Ca_{1/3}Fe_{2/3}Co_{2/3}Cu_{2/3}O_{5+\delta}$ (NBSC) and $NdBa_{1/4}Sr_{1/4}Ca_{1/4}Mg_{1/4}Fe_{2/3}Co_{2/3}Cu_{2/3}O_{5+\delta}$ (NBSCM) were prepared via nitrate-citrate method [31] using as starting reagents the citric acid hydrate (CA) $C_6H_8O_7 \cdot H_2O$ (pure), $Ba(NO_3)_2$ (pure), $Sr(NO_3)_2$ (analytical grade), $Ca(NO_3)_2 \cdot 4H_2O$ (pure), $Mg(NO_3)_2 \cdot 6H_2O$ (analytical grade), $Fe(NO_3)_3 \cdot 6H_2O$ (analytical grade), $Co(NO_3)_2$ (analytical grade), as well as Nd_2O_3 (pure) and CuO (analytical grade), hereby the last two chemicals were preliminary dissolved in the concentrated nitric acid (special pure grade). The solutions of different metals (C_i = 0.3–0.6 M) were mixed to obtain resulting solutions with corresponding stoichiometric ratios of metals, then to this mixture the CA solution (C_{CA} = 0.6–0.8 M) in appropriate quantity ($\Sigma n_{Me} : n_{CA} = 1 : 1.3$) was added and final mixture was heated at stirring on an IKA RH basic 2 magnetic stirrer until a viscous brown gel formed.

Then the gel was dried in an furnace oven at 130–200 ºC at slow temperature gaining. Near 180–200 ºC took place selfignition of resulting mass with formation of dark brown powder. This powder was annealed in air in an electrical oven at 600 ºC for 4 h, after which it was ground in an agate mortar and pressed into pellets with diameter of 15 mm and height of 3–5 mm, that were additionally annealed at 900 ºC in air for 8 h. After that black pellets were reground in an agate mortar, pressed into bars

with dimensions of 5 × 5 × 30 mm and sintered in air at 1000 ºC for 9 h.

Characterization

X-ray patterns of the powdered samples were recorded using a Bruker D8 XRD Advance diffractometer (Bruker, USA) (CuKα – radiation, Ni–filter). The lattice constants of the samples were calculated using RTP 4.5 software [32] and refined using Rietveld method with the Fullprof 3.0 software [33]. To study bond energies was used IR absorption spectrometer Nexus E.S.P. (ThermoScientific, USA), mixtures of powders and KBr (99.9%) were prepared for analysis.

Oxygen nonstoichiometry index (δ) of the samples was determined iodometrically [34]. The values of coherent scattering areas (CSAs, D) and microstrains (ε) were estimated using Sherrer equation (D_S), Williamson–Hall ($D_{W–H}$), and size–strain methods ($D_{S–S}$), as it was described earlier [30].

Apparent density values (ρ_{app}) of the sintered ceramics were determined based on its mass and geometrical dimensions. Porosity (P) values of ceramics were calculated using equation:

$$P = (1 - \frac{\rho_{app}}{\rho_{XRD}}) \times 100\%,$$

where ρ_{XRD} is the X-ray density of the samples.

The microhardness of ceramics was measured via Vickers method using microhardness meter AFFRI-MVD M8 (AFFRI, Italy).

Thermal stability of powdered samples was studied in air within 300–1100 K temperature range using a TGA/DSC-1/1600 HF thermoanalytical system (Mettler Toledo Instruments, Switzerland). Thermal expansion of sintered ceramics was investigated in air within 300–1100 K temperature interval with a DIL 402 PC quartz dilatometer (Netzsch, Germany). Average LTEC values (α) were calculated from the linear parts of the $\Delta l/l_0 = f(T)$ dependences. Isolation of the thermal and chemical contributions into sample expansion was carried out using methodics described in [30].

Electrical conductivity (σ) and Seebeck coefficient (S) of the ceramic samples were determined in air within temperature interval of 300–1100 K [35]. Apparent activation energies of electrical conductivity (E_σ) and thermo-EMF (E_S) were calculated from the linear parts of $\ln(\sigma \cdot T) = f(1/T)$ and $S = f(1/T)$ dependences respectively. Assuming that conductivity character of the samples studied has a hopping nature (with small-radius polarons as charge carriers) [36–38], values of activation energy of polarons (E_A) and activation energy of their motion (E_m) were calculated as $E_A = E_S$, $E_m = E_\sigma - E_A = E_\sigma - E_S$.

Values of weighted mobility of charge carriers (μ) and their concentration (p) were calculated using experimentally obtained σ and S values through method described in [39]. Activation energy of charge carriers (E_p) was found from linear part of $\ln(p) = f(1/T)$ dependences.

Results and discussion

Crystal structure end oxygen content

At 1000 ºC the NB and NBS samples crystallized in the tetragonal symmetry (space group $P4/mmm$), while the NBSC and NBCSM – in the cubic one (space group $Pm3m$). The X-ray diffraction patterns of all samples showed low-intensity peaks from impurity phases (Fig. 1a), which were identified by us as so-called Nd_2BaCuO_5 "brown phase", $BaCoO_3$, $BaFeO_3$, Fe_3O_4, Co_3O_4 etc. (JCPDS ICDD PDF-2). It is worth noting that the content of impurity phases is lower in the NBSC and NBSCM samples compared to the others. This suggests that the high CE value stabilizes the crystal structure of these samples. The change in crystal structure is due to compression of the unit cell (Table 1), as parameters such as a, c, etc., decreased upon substitution of larger barium cations ((in 6-fold coordination $R_{Ba^{2+}} = 1.35$ Å) by smaller strontium, calcium, and magnesium ones ($R_{Sr^{2+}} = 1.18$ Å, $R_{Ca^{2+}} = 1.00$ Å, $R_{Mg^{2+}} = 0.72$ Å [40]).

The compression of the unit cell has also been confirmed by IR absorption spectroscopy. Three absorption bands were observed in the spectra of the powder samples: 494–499 cm^{-1} (ν_1), 537–567 cm^{-1} (ν_2) and 618 cm^{-1} (ν_3) (Fig. 1b). These correspond to the stretching vibrations of the (Fe,Co,Cu)–O–(Fe,Co,Cu) bonds in the [(Fe,Co,Cu)O_2] layers (ν_1 and ν_2) of the crystal structure of NBS, and in the direction perpendicular to these layers (ν_3) [41].

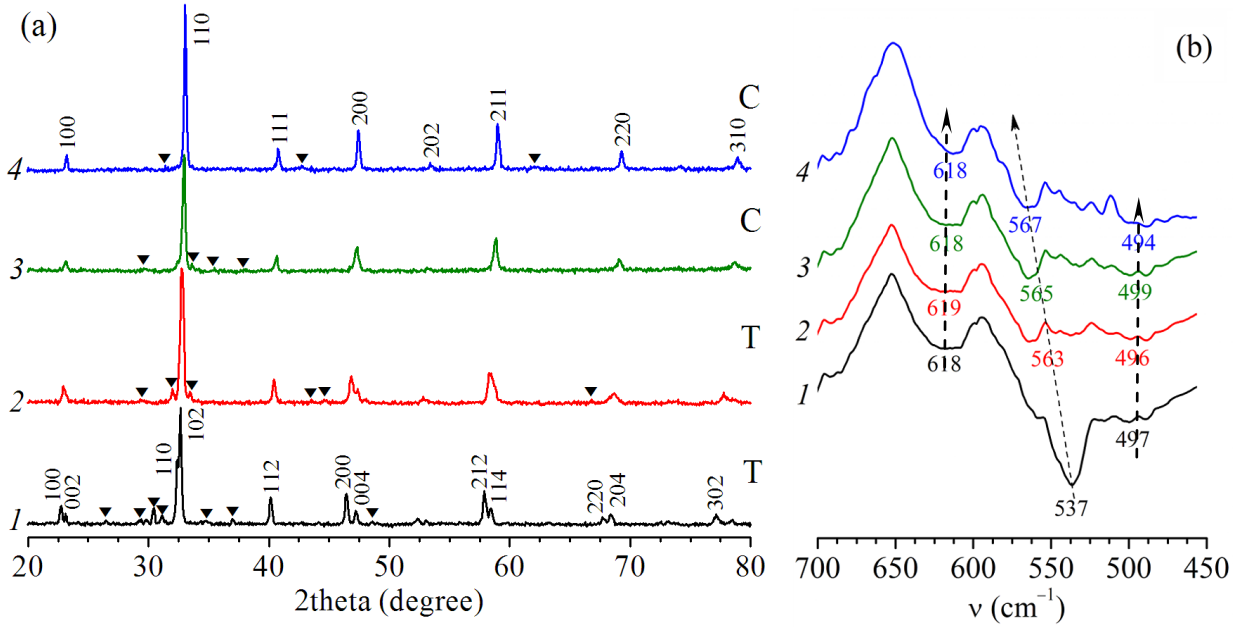


Figure 1. X-ray diffraction patterns (a) and IR absorption spectra (b) of Nd(Ba,Sr,Ca,Mg)$Fe_{2/3}Co_{2/3}Cu_{2/3}O_{6-\delta}$ powdered samples: NB (*1*), NBS (*2*), NBSC (*3*), NBSCM (*4*). (T – tetragonal phase, C – cubic phase). ▼ – impurity phases

As can be seen in fig. 1b, there is a shift of band (ν_2) to higher frequencies, which this correlates with the decrease in the structural parameter *a* (Table 1). The positions of (ν_1) and (ν_3) bands remained nearly constant (fig. 1,b), which correlated with the fact that *c* parameter of crystal structure of Nd(Ba,Sr,Ca,Mg)$Fe_{2/3}Co_{2/3}Cu_{2/3}O_{6-\delta}$ samples slightly changed at variation of their chemical composition (Table 1).

Table 1. Space group, lattice constants (*a*, *c*, *V*, a_p), axial ratio (*c*/2*a*), oxygen nonstoichiometry index (δ) and fitting parameters (χ^2, R_B) of Nd(Ba,Sr,Ca,Mg)$Fe_{2/3}Co_{2/3}Cu_{2/3}O_{6-\delta}$ solid solutions

x	Space group	δ	*a*, Å	*c*, Å	a_p, Å	*V*, Å^3	*c*/2*a*	χ^2	R_B, %
NB	*P*4/*mmm*	0.38	3.9122	7.6963	3.8907	117.796	0.9836	0.185	5.19
NBS	*P*4/*mmm*	0.18	3.8828	7.6870	3.8697	115.889	0.9899	0.393	5.05
NBSC	*Pm*3*m*	0.21	3.8456	–	3.8456	56.871	–	0.246	2.38
NBSCM	*Pm*3*m*	0.19	3.8357	–	3.8357	56.431	–	0.252	2.89

The deficiency of weakly bounded oxygen in the samples when barium was replaced by strontium, calcium and magnesium decreased from 0.38 to 0.18–0.21. Considering the error of the determination method (0.2%), the δ values for the all substituted samples were identical.

Microstructure

After sintering, the samples with different crystal symmetries had fundamentally different porosities and apparent densities. The

NB and NBS samples had the highest porosity (P = 25–30%), while the NBSC and NBSCM samples had lower ones (P < 10%) (Table 2). The NBSC and NBSCM samples also had the highest microhardness values (880–1120 HV). Comparison of these values suggests that the high CE values of the NBSC and NBSCM samples significantly improve the sintering ability of the ceramics.

The values of the CSAs for all calculation methods changed in a non-monotonic manner in the ranges of D_S = 26–34 nm, $D_{W–H}$ = 31–50 nm, and $D_{S–S}$ = 28–39 nm (Table 2), and were minimal for the NBS and NBSC samples. The microstresses in the samples decreased significantly (Table 2) with increasing substitution degree (especially in the size–strain method), which is due to changes in the symmetry of the crystal structure (from a tense tetragonal to a more symmetric cubic structure) and a high-entropy stabilizing factor [27].

Table 2. Apparent density (ρ_{app}), porosity (P), microhardness (HV100, under 100 kgf/mm^2), coherent scattering area (D) and microstrains (ε) calculated using Sherrer, Williamson–Hall and size–strain methods for Nd(Ba,Sr,Ca,Mg)$Fe_{2/3}Co_{2/3}Cu_{2/3}O_{6-\delta}$ sintered ceramics

x	ρ_{app}, г/см^3	P, %	HV100	Sherrer	Williamson–Hall		Size–strain	
				D_S, nm	$D_{W–H}$, nm	$10^3\cdot\varepsilon$	$D_{S–S}$, nm	$10^3\cdot\varepsilon$
NB	5.06	27.2	154.5	31	50	3.09	39	8.58
NBS	4.32	35.6	133.3	26	31	2.34	28	6.94
NBSC	5.89	9.16	880.4	29	38	1.47	29	1.53
NBSCM	5.82	7.68	1127	34	41	1.49	36	4.00

Thermal properties

In the 300–1100 K temperature range, all samples were thermally stable and did not decomposes into more simple ternary, binary etc. oxides. However, at temperatures of T^* = 560–680 K, the samples began to lose weight (0.52–0.95 %), which was associated with the release of weakly bound oxygen (Fig. 2). The temperatures at which mass loss began for samples with high CE values (NBSC and NBSCM) were higher (Fig. 2, top inset) than for others, and the amount of oxygen released in the T^*–1100 K temperature interval ($\Delta\delta$) for tetragonal samples was equal 0.59–0.65, while for cubic ones was equal 0.42–0.44, which was essentially smaller. Based on these findings, we can conclude that the medium-entropy oxides NBSC and NBSCM have better thermal stability are lose oxygen more slowly than other samples.

The $\Delta l/l_0 = f(T)$ dependences of the NB and NBSCM samples exhibit a kink at temperatures of $T^{\#}$ = 630 and 950 K, respectively (Fig. 2b). After this point, there is a sharp increase in the LTEC of the samples. This increase is due to the release of weakly bounded oxygen from the samples at high temperatures. The LTECs in all studied temperature ranges (α) (T = 350–1070 K), both before (α_T – thermal expansion) and after the kink point (α_2) ($T^{\#}$), as well as the chemical expansion coefficients (α_δ) are shown on Fig. 2b for the NB and NBSCM samples. As one can see, the thermal expansion decreases by 7 % with increasing CE value, while the average LTEC decreases by 13 %. On the contrary, the chemical expansion increases from $6.21\cdot10^{-3}$ to $11.0\cdot10^{-3}$ with increasing CE value.

It is interesting to note that, as with mass loss, the temperature of the kink points also increases. The $T^{\#}$ for the NBSCM sample was 950 K, allowing this composition to be used as a cathode material with a reduced LTEC value in the intermediate temperature range (700–1000 K). Unfortunately, before the kink point, the LTEC value of NBSCM sample is still high and is equal to $16.2\cdot10^{-6}$ K^{-1}, making it unsuitable for practical use as a SOFC cathode. However, these studies demonstrate that the entropy factor positively affects the LTEC of ceramics, proving the success of this approach in improving the properties of layered perovskites.

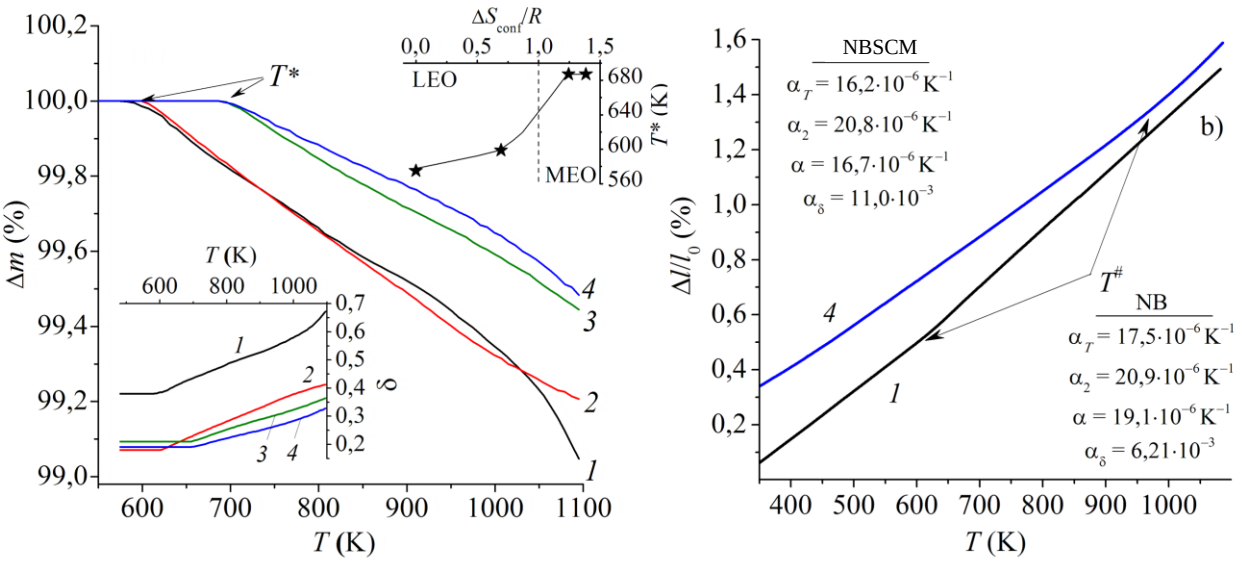


Figure 2. Temperature dependences of the mass loss (a) and relative elongation (b) for the Nd(Ba,Sr,Ca,Mg)$Fe_{2/3}Co_{2/3}Cu_{2/3}O_{6-\delta}$ layered perovskites: NB (*1*), NBS (*2*), NBSC (*3*), NBSCM (*4*) (dilatometric curve *4* is shifted vertically by 0.1%). Insets show dependences of oxygen nonstoichiometry index of the samples versus temperature (bottom) and temperatures of mass loss beginning versus ΔS_{conf} values (top)

Electrotransport properties

In the temperature range of 300–1100 K, the conductivity of the NB and NBS samples initially had a semiconductor character ($\partial\sigma/\partial T > 0$), which changed into a metal-like one ($\partial\sigma/\partial T < 0$) near T = 690 K (Fig. 3a). This transition is associated with the release of weakly bounded oxygen resulting in the decrease of the main charge carriers ("holes") concentration in the samples. The NBSC and NBSCM samples showed a semiconductor-like dependence in the entire temperature range studied. The lack of maxima on the $\sigma = f(T)$ curves for these solid solutions can be due to the fact that they possessed higher oxygen content which change at heating is insufficient to essentially decrease main change carriers' concentration in them. The other case is that due to the relatively low porosity of these samples the oxygen evolution from them into environment is hindered and concentration of main charge carriers ("holes") remains practically unchanged at least at intergrains which state governs the transport properties of the layered perovskites.

The Seebeck coefficient values of the samples were positive over the entire temperature range, indicating that main charge carriers in the samples are "holes". On the $S = f(T)$ dependence for all samples, a minimum was found at temperatures in the range T = 630–1000 K (Fig. 4b). The temperature of the minimum increased with increasing CE value and was significantly higher for the NBSC and NBSCM samples (915 and 1000 K, respectively) compared to NB and NBS ones (630 and 665 K, respectively).

At temperatures below the onset of oxygen evolution ($\leq$ 650 K), the electrical conductivity of the samples showed non-monotonic variation with composition of the samples (Table 3). For example, at 550 K, the σ ranged from 39.7 to 66.2 S/cm. Generally, the conductivity increased, which can be attributed to an increase in charge carriers' mobility (μ_W) (Table 3). A high σ value for the NBS sample can be explained by a high charge carrier concentration at that temperature ($p_{550} = 123 \cdot 10^{19}$ cm^{-3}), which is significantly higher than the p values of other compositions ($(27–54) \cdot 10^{19}$ cm^{-3}). The S values of all compositions also showed non-monotonic behavior before the minimum on the $S = f(T)$ dependences (Table 3).

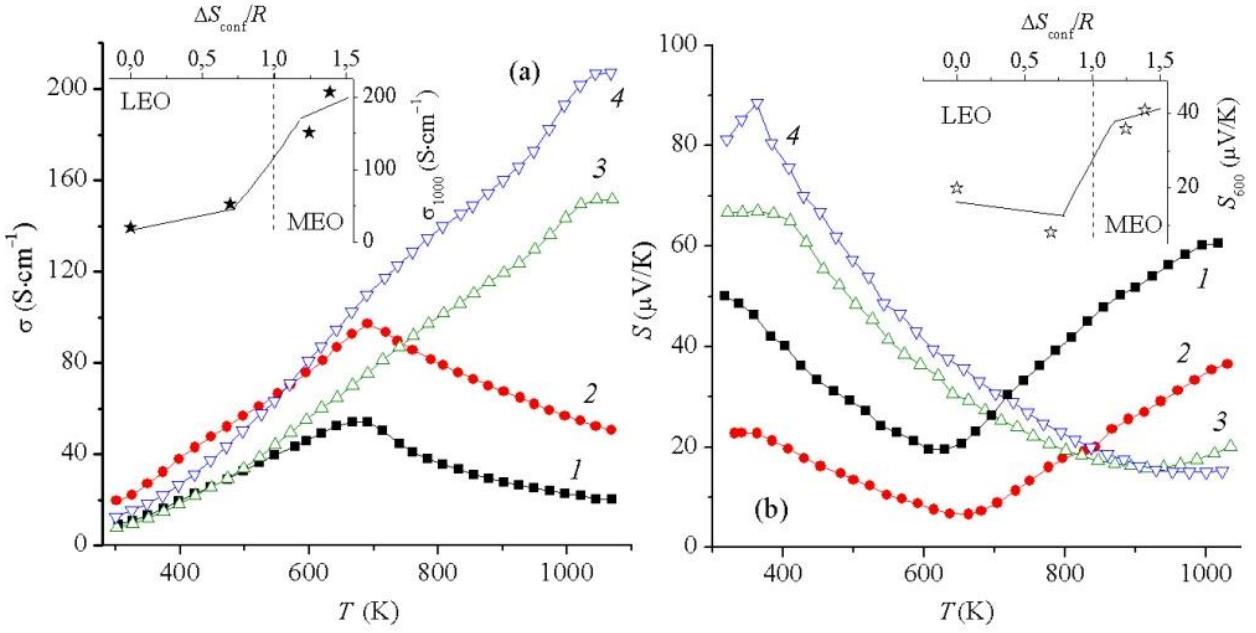


Fig. 3. Temperature dependences of electrical conductivity (a) and Seebeck coefficient (b) of the Nd(Ba,Sr,Ca,Mg)$Fe_{2/3}Co_{2/3}Cu_{2/3}O_{6-\delta}$ ceramic samples: NB (*1*), NBS (*2*), NBSC (*3*), NBSCM (*4*). Insets show dependences of values σ (Fig. 3a) and *S* (Fig. 3b) at 1000 K versus ΔS_{conf} values

In the high temperature region (> 650 K), the σ and *S* values showed a monotonic change in the solid solutions series. Additionally, the high oxygen content (6–δ) and, as one can see in inset on Fig. 3a, mostly the CE values contributed to the increase in electrical conductivity values. The NBSCM sample exhibited the highest electrical conductivity, with a value of σ = 200 S/cm at 1015 K, which is about 9.5 times larger than the electrical conductivity of the base composition, NB, at the same temperature (21 S/cm). The *S* values also decreased from 61 μV/K for NB to 15 μV/K for NBSCM at the same temperature.

Table 3. Values of activation energies of electrotransport (E_σ, E_S, E_m, E_p) within temperature range 350–650 K, electrical conductivity (σ_{550}), Seebeck coefficient (S_{550}), weighted mobility (μ_{W550}) and concentration (p_{550}) of the charge carriers at 550 K for Nd(Ba,Sr,Ca,Mg)$Fe_{2/3}Co_{2/3}Cu_{2/3}O_{6-\delta}$ ceramics

x	E_σ, eV	E_S, eV	E_m, eV	E_p, eV	σ_{550}, S/cm	S_{550}, μV/K	μ_{W550}, $cm^2/(V\cdot s)$	$p_{550}\cdot10^{19}$ cm^{-3}
NB	0,091	0,023	0,068	0,172	39.7	23.8	0.46	54.3
NBS	0,073	0,013	0,060	0,153	66.2	10.5	0.34	123
NBSC	0,112	0,038	0,074	0,124	44.9	41.1	0.91	26.8
NBSCM	0,107	0,042	0,065	0,136	64.5	47.6	1.52	31.1

As can be seen from the Table 3, activation energy of polarons in the samples studied (E_A) increased about 2 times at transition from NB and NBS (tetragonal perovskites, LEO (BS)) to the NBSC and NBSCM ones (cubic perovskites, MEO (BS)), whereas activation energy of their motion (E_m) remains practically the same and equal to 0.06-0.07 eV. Activation energy of charge carriers ("holes") (E_p), in the whole, decreased at increasing of CE values of ceramics (Table 3) from 0.172 eV for NB complex oxide to 0.136 eV for NBSCM phase. Weighted mobility values of the charge carriers increased at CE increasing and for MEO (BS) (cubic phases) were more than 2 times larger than for LEO (BS) ones (tetragonal phases), and the largest value (1.52 $cm^2/(V\cdot s)$ at 550 K) was found for

the NBSCM sample possessing the largest CE value among the samples studied (Table 3).

Conclusions

Medium-entropy $Nd(Ba,Sr,Ca,Mg)Fe_{2/3}Co_{2/3}Cu_{2/3}O_{6-\delta}$ solid solutions with partial substitution of barium by strontium, calcium and magnesium were obtained using the nitrate-citrate synthesis method. The effect of this substitution, as well as the configurational entropy value, on the crystal structure, microstructure, thermal properties (thermal stability and thermal expansion) and electrical transport properties (electrical conductivity and thermoelectric power) of the ceramics were studied.

It was found that the NB and NBS samples had a tetragonal structure (space group *P*4/*mmm*), and NBSC and NBSCM samples had a cubic one (space group *Pm*3*m*). Substituting of barium by strontium, calcium and magnesium reduced the crystal structure parameters, decreased the microstresses in the grains of ceramics and deficiency of weakly bounded oxygen. High entropy of the system led to a denser microstructure of the samples with lower porosity and higher microhardness. This also improved thermal stability and decreased the LTEC value, as well as increased electrical conductivity, while the Seebeck coefficient is decreased. Overall, the analysis of these data suggests that configurational entropy has a positive impact on the structure, sinterability, thermal and electrical properties of the layered perovskites.

Among all the studied samples, the NBSCM composition with the highest entropy ($\Delta S_{conf} = 1.38R$) had the highest thermal stability and electrical conductivity (200 S/cm at 1015 K) and the latter is provided by the high mobility values of charge carriers in it. This sample also had a lower average LTEC value ($16.2 \cdot 10^{-6}$ K^{-1}) over a wide temperature range of $T = 350–950$ K. These characteristics make the $NdBa_{1/4}Sr_{1/4}Ca_{1/4}Mg_{1/4}Co_{2/3}Fe_{2/3}Cu_{2/3}O_{5+\delta}$ composition the promising cathode material for SOFCs operating in the intermediate temperature range.

Acknowledgements

Ya. Yu. Zhuravleva acknowledges financial support by the Ministry of Education of the Republic of Belarus (project 20240718 from 26.04.2024). A.I. Klyndyuk acknowledges financial support by the Belarusian Republican Foundation for Fundamental Research (grant C26CH-028).

References

1. Reghunadhan A., Ajitha A.R. *Chapter 12 - Development of perovskite nanomaterials for energy applications* / Editor(s): Sabu Thomas, Nandakumar Kalarikkal, Ann Rose Abraham. In Micro and Nano Technologies, Design, Fabrication, and Characterization of Multifunctional Nanomaterials: Elsevier, 2022, P. 269–294.
2. Seikh M.M., Pralong V., Lebedev O.I., Caignaert V., Raveau B. The ordered double perovskite $PrBaCo_2O_6$: Synthesis, structure, and magnetism. *J. Appl. Phys.* 2013. V. 114. No. 1. P. 013902.
3. Pang S., Xu J., Su Y. et al. The role of A-site cation size mismatch in tune the catalytic activity and durability of double perovskite oxides. *Appl. Cata. B: Environ.* 2020. V. 270. P. 118868.
4. Teketel B.S., Beshiwork B.A., Tian D. et al. Promoted Performance of Layered Perovskite $PrBaFe_2O_{5+\delta}$ Cathode for Protonic Ceramic Fuel Cells by Zn Dopin. *Catalysts.* 2022. V. 12. No. 5. P. 488.
5. Tarasova N.A., Animitsa I.E., Galisheva A.O., Medvedev D.A. Layered and hexagonal perovskites as novel classes of proton-conducting solid electrolytes. A focus review. *Electrochem. Mater. Tech.* 2022. V. 1. No. 1. P. 20221004.
6. Zhu X., Pan X., Wu Y. et al. Layered perovskite oxide $PrBaCo_2O_{5+\delta}$ as a potential cathode for lithium–oxygen batteries: High-performance bi-functional electrocatalysts. *Mater. Lett.* 2019. V. 237. P. 200–203.
7. Abanti N., Shubha V. Oxide Thermoelectric Materials: A Structure-Property Relationship. *J. Electronic Mater.* 2014. V. 43. No. 4. P. 962–977.
8. Im J.M., Schlegl H., Park J.-Y., Baek S.-W., Kim J.H. Electrochemical properties of B-site

non-stoichiometric layered perovskite $SmBa_{0.5}Sr_{0.5}Co_xO_{5+\delta}$ (x = 1.9–2.1) cathodes for IT-SOFC. *Ceram. Int.* 2024. V. 50. No. 13, Part B. P. 24565–24575.
9. Chen F., Zhou D., Xiong X. et al. Doping strategy on improving the overall cathodic performance of double perovskite $Ln BaCo_2O_{5+\delta}$ (*Ln* = Pr, Gd) as potential SOFC cathode materials. *J. Materiom.* 2023. V. 9.No. 5. P. 825–83.
10. Khandale A.P., Kumar R.V., Bhoga S.S. Effect of synthesis route on electrochemical performance of $PrBaCo_2O_{5+\delta}$ cathode for IT-SOFC application. *Bull. Mater. Sci.* 2023.V. 46. P. 119.
11. Chroneos A., Goulatis I.L, Solovjov A, Vovk R.V. The Evolution of Solid Oxide Fuel Cell Materials. *Appl. Sci.* 2024. V. 14. No. 1. P. 69.
12. Klyndyuk A.I., Chizhova E.A., Kharytonau D.S., Medvedev D.A. Layered Oxygen-Deficient Double Perovskites as Promising Cathode Materials for Solid Oxide Fuel Cells. *Materials.* 2022. V. 15. No. 1. P. 141.
13. Zheng F., Pang S. Progress in Developing $LnBaCo_2O_{5+\delta}$ as an Oxygen Reduction Catalyst for Solid Oxide Fuel Cells. *Catalysts.* 2023. V. 13. P. 1288.
14. Kharton V.V., Marques F.M.B., Atkinson A. Transport properties of solid oxide electrolyte ceramics: A brief review. *Solid State Ion.* 2004. V. 174. No.1–4. P. 135–149.
15. Pan J., Chen X., Cai D. et al. Iron-doped perovskite $La_{0.5}Pr_{0.5}BaCo_{2-x}Fe_xO_{5+\delta}$ as a potential cathode material for SOFC. *Ceram. Int.* 2025. V. 51. No. 8. P. 10703–10715.
16. Zhang Y., Yu B., Lü S. et al. Effect of Cu doping on $YBaCo_2O_{5+\delta}$ as cathode for intermediate-temperature solid oxide fuel cells. *Electrochim. Acta.* 2014. V. 134. P. 107–115.
17. Liu L., Guo R., Wang S., Yang Y., Yin D. Synthesis and characterization of $PrBa_{0.5}Sr_{0.5}Co_{2-x}Ni_xO_{5+\delta}$ (x = 0.1, 0.2 and 0.3) cathodes for intermediate temperature SOFCs. *Ceram. Int.* 2014. V. 40. P. 16393–16398.
18. Baek K.S., Baek S.-W., Kang H. et al. Electrical conductivity characteristics of Sr substituted layered perovskite cathode ($SmBa_{0.5}Sr_{0.5}Co_2O_{5+\delta}$) for intermediate temperature-operating solid oxide fuel cell. *Ceram. Int.* 2022. V. 48. No. 11. P. 15770–15779.
19. Li J., Sun N., Liu X. et al. Investigation on $Nd_{1-x}Ca_xBaCo_2O_{5+\delta}$ double perovskite as new oxygen electrode materials for reversible solid oxide cells. *J. Alloy. Compd.* 2022. V. 913. P. 165245.
20. Chen F., Zhou D., Xiong X. et al. Doping strategy on improving the overall cathodic performance of double perovskite $Ln BaCo_2O_{5+\delta}$ (*Ln* = Pr, Gd) as potential SOFC cathode materials. *J. Materiom.* 2023. V. 9. No. 5. P. 825–837.
21. Woo S.H., Song K.E., Baek S.-W. et al. Pr- and Sm-Substituted Layered Perovskite Oxide Systems for IT-SOFC Cathodes. *Energies.* 2021. V. 14. P. 6739.
22. Ling Y., Han X., Yang Y. et al. Stable High-Entropy Double Perovskite Cathode $SmBa(Mn_{0.2}Fe_{0.2}Co_{0.2}Ni_{0.2}Cu_{0.2})_2O_{5+\delta}$ for Intermediate-Temperature Solid Oxide Fuel Cells. *J. Chinese Ceram. Soc.* 2022. V. 50.No. 1. P. 219.
23. Guo T., Dong J., Chen Z. et al. Enhanced Compatibility and Activity of High-entropy Double Perovskite Cathode Material for IT-SOFC. *J. Inorg. Mater.* 2022. V. 38. P. 551.
24. Yu J., Luo L., Cheng L. et al. A-Site Engineering of the High-Entropy Perovskite $Pr_{0.4}La_{0.4}Ba_{0.4}Sr_{0.4}Ca_{0.4}Fe_2O_{5+\delta}$ Cathode for Intermediate-Temperature SOFCs. ACS Appl. *Mater. Interfaces.* 2024. V. 16. No. 29.P. 36224–36235.
25. Zhang Z., Wang H., Li X., Xu H., Qi M. CO_2/Cr-tolerance and oxygen reduction reaction of novel high-entropy perovskite cathode for intermediate temperature solid oxide fuel cell. *Ceram. Int.* 2024. V. 50. No. 7, Part B. P. 11360–11369.
26. Pikalova E.Y., Kalinina E.G., Pikalova N.S., Filonova E.A. High-Entropy Materials in SOFC Technology: Theoretical Foundations for Their Creation, Features of Synthesis, and Recent Achievements. *Materials.* 2022. V. 15. No. 24. P. 8783.
27. Sarkar A., Wang Q., Schiele A. et al. High-Entropy Oxides: Fundamental Aspects and Electrochemical Properties. *Adv. Mater.* 2019. V. 31, No. 26. P. e1806236.
28. Klyndyuk A.I., Zhuravleva Ya.Yu. Structure and Physicochemical Properties of Solid Solutions $NdBa_{1-x}Ca_xFeCo_{0,5}Cu_{0,5}O_{5+\delta}$ ($0{,}00 \le x \le 0{,}40$). *Russ. J. of Inorg. Chem.* 2022. V. 67. No. 12. P. 2084–2089.
29. Chizhova E.A., Klyndyuk A.I., Zhuravleva Ya.Yu., Shevchenko S.V. Electrical Transport and Thermal Properties of $NdBa_{1-}$

$_x$Mg$_x$FeCo$_{0,5}$Cu$_{0,5}$O$_{5+\delta}$ ($0{,}00 \le x \le 0{,}40$) Solid Solutions. *Glass Phys. Chem.* 2023. V. 49. No. 1. P. 57–62.
30. Zhuravleva Ya.Yu., Klyndyuk A.I., Tugova E.A., Gundilovich N.N., Tomkovich M.V. Structural, thermal and electrical properties of the ceramics in the NdBaFe$_{2/3}$Co$_{2/3}$Cu$_{2/3}$O$_{6-\delta}$–NdSrFe$_{2/3}$Co$_{2/3}$Cu$_{2/3}$O$_{6-\delta}$ system. *Solid State Sciences*. 2025. V. 163. P. 107906.
31. Klyndyuk A.I., Matsukevich I.V. Synthesis and Properties of Disubstituted Derivatives of Layered Calcium Cobaltite. *Glass Phys. Chem.* 2015. V. 41. No. 5. P. 545–550.
32. Tabular processor for X-ray diffractometry RTP 4.5. URL: slavic.me/rtp/index.htm.
33. Rietveld H.M. A profile refinement method for nuclear and magnetic structures, *J. Appl. Crystallogr.* 1969. V. 2. No. 2. P. 65–71.
34. Urusova A.S., Cherepanov V.A., Aksenova T.V., Gavrilova L.Ya., Kiselev E.A. Phase equilibria, crystal structure and oxygen content of intermediate phases in the Y–Ba–Co–O system. *J. Solid State Chem.* 2013. V. 202. P. 207–214.
35. Klyndyuk A.I., Chizhova E.A. Structure, Thermal Expansion, and Electrical Properties of BiFeO$_3$–NdMnO$_3$ Solid Solutions. Inorg. Mater. 2015. V. 51. P. 272–277.
36. Bao X., Su X., Wang S. et al. Effects of Bi-doping on structure and properties of YBaCo$_2$O$_{5+\delta}$ layered perovskite cathode for intermediate-temperature solid oxide fuel cells. *J. Alloy. Compd.* 2023. V. 965. P. 171391.
37. Klyndyuk A.I., Kharytonau D.S., Mosiałek M. et al. Double-substituted NdBa(Fe,Co,Cu)$_2$O$_{5+\delta}$ layered perovskites as cathode materials for intermediate-temperature solid oxide fuel cells – correlation between structure and electrochemical properties. *Electrochim. Acta.* 2022. V. 411. P. 140062.
38. Mott N., Davis E. *Electronic Processes in Non-Crystalline Materials*, Oxford: Oxford Univ. Press, 1989, 2nd ed
39. Snyder G.J., Snyder A.H., Wood M. et al. Weighted Mobility. *Adv. Mater.* 2020. V. 35. P. 200153.
40. Shannon R.D. Revised effective ionic radii and systematic studies of interatomic distances in halides and chalcogenides. *Acta Crystallogr. Sect. A: Cryst. Phys., Diffr. Theor. Gen. Crystallogr.* 1976. V. 32. No. 5. P. 751–767.
41. Klyndyuk A.I., Chizhova E.A. Properties of perovskite-like phases *Ln*BaCuFeO$_{5+\delta}$ (*Ln* – La, Pr). *Glass Phys. Chem*. 2008. V. 34. P. 313–318.

Laylı Nd(Ba,Sr,Ca,Mg)(Fe,Co,Cu)$_2$O$_{6-\delta}$ PEROVSKITLƏR: KONFIQURASIYA ENTROPIYASININ STRUKTUR VƏ XASSƏLƏRƏ TƏSIRI

Ya.Yu. Zhuravleva, E.A. Chizhova, A.S. Hlinski, A.I. Klyndyuk

Nitrat-sitrat metodundan istifadə edərək, entropiya ilə sabitləşdirilmiş barium və kobalt alt qəfəsləri olan laylı neodim-barium-kobaltit törəmələri sintez edilmişdir. Onların kristal quruluşu, oksigen qeyri-stexiometriyası, mikrostrukturu, istilik, mexaniki və elektronəqliyyat xüsusiyyətləri öyrənilmişdir. Barium alt qəfəsinin (BS) konfiqurasiya entropiyasının (CE) artmasının perovskit vahid hüceyrəsinin ölçüsünün azalmasına, nümunələrin oksigen çatışmazlığının, məsaməliliyinin, istilik genişlənməsinin xətti əmsalının (LCTE, αT) və Seebeck əmsalının azalmasına, eləcə də onların mikrosərtliyinin, istilik stabilliyinin və elektrik keçiriciliyinin artmasına səbəb olduğu aşkar edilmişdir ki, bu da ən çox aşağı entropiyalı (LE) BS-dən orta entropiyalı (ME) BS-ə keçiddə özünü göstərir. NdBa$_{1/4}$Sr$_{1/4}$Ca$_{1/4}$Mg$_{1/4}$Fe$_{2/3}$Co$_{2/3}$Cu$_{2/3}$O$_{6-\delta}$ birləşməsi ən yüksək elektrik keçiriciliyi və ən aşağı LTEC dəyərini nümayiş etdirir, ən yüksək CE 1015 K-də ≈200 S sm^{-1} və 350–1070 K temperatur diapazonunda 16.2 10^{-6} K^{-1} təşkil edir ki, bu da laylı perovskit NdBaFe$_{2/3}$Co$_{2/3}$Cu$_{2/3}$O$_{6-\delta}$ -dən müvafiq olaraq təxminən 10 dəfə yüksək və 13% aşağıdır.

Açar sözlər: Laylı perovskitlər, Konfiqurasiya entropiyası, Oksigen qeyri-stexiometriyası, İstilik genişlənməsi, Elektrik keçiriciliyi, Seebeck əmsalı